Research Article | Vol. 9, No. 3 | 1 Mar 2018 | BIOMEDICAL OPTICS EXPRESS 1375
Biomedical Optics EXPRESS

Quantitative evaluation of redox ratio and collagen characteristics during breast cancer chemotherapy using two-photon intrinsic imaging

SHULIAN WU,[1,2,4] YUDIAN HUANG,[3,4] QINGGONG TANG,[2] ZHIFANG LI,[1] HANNAH HORNG,[2] JIATIAN LI,[1] ZAIHUA WU,[3] YU CHEN,[1,2,5] AND HUI LI[1,6]

[1]*College of Photonic and Electronic Engineering, Fujian Normal University, Fujian Provincial Key Laboratory of Photonic Technology, Key Laboratory of Optoelectronic Science and Technology for Medicine, Ministry of Education, Fuzhou, Fujian, 350007, China*
[2]*Fischell Department of Bioengineering, University of Maryland, College Park, MD, 20742, USA*
[3]*Department of Pathology, Fuzhou First Hospital Affiliated to Fujian Medical University, Fuzhou, Fujian, 350009, China*
[4]*These authors contributed equally to this work.*
[5]*yuchen@umd.edu*
[6]*hli@fjnu.edu.cn*

Abstract: Preoperative neoadjuvant treatment in locally advanced breast cancer is recognized as an effective adjuvant therapy, as it improves treatment outcomes. However, the potential complications remain a threat, so there is an urgent clinical need to assess both the tumor response and changes in its microenvironment using non-invasive and precise identification techniques. Here, two-photon microscopy was employed to detect morphological alterations in breast cancer progression and recession throughout chemotherapy. The changes in structure were analyzed based on the autofluorescence and collagen of differing statuses. Parameters, including optical redox ratio, the ratio of second harmonic generation and auto-fluorescence signal, collagen density, and collagen shape orientation, were studied. Results indicate that these parameters are potential indicators for evaluating breast tumors and their microenvironment changes during progression and chemotherapy. Combined analyses of these parameters could provide a quantitative, novel method for monitoring tumor therapy.

OCIS codes: (170.3880) Medical and biological imaging; (180.4315) Nonlinear microscopy; (100.2960) Image analysis.

References and links

1. R. L. Siegel, K. D. Miller, and A. Jemal, "Cancer statistics, 2016," CA Cancer J. Clin. **66**(1), 7–30 (2016).
2. C. E. DeSantis, F. Bray, J. Ferlay, J. Lortet-Tieulent, B. O. Anderson, and A. Jemal, "International variation in female breast cancer incidence and mortality rates," Cancer Epidemiol. Biomarkers Prev. **24**(10), 1495–1506 (2015).
3. C. Liedtke, C. Mazouni, K. R. Hess, F. André, A. Tordai, J. A. Mejia, W. F. Symmans, A. M. Gonzalez-Angulo, B. Hennessy, M. Green, M. Cristofanilli, G. N. Hortobagyi, and L. Pusztai, "Response to neoadjuvant therapy and long-term survival in patients with triple-negative breast cancer," J. Clin. Oncol. **26**(8), 1275–1281 (2008).
4. C. Jackisch, F. A. Scappaticci, D. Heinzmann, F. Bisordi, T. Schreitmüller, G. Minckwitz, and J. Cortés, "Neoadjuvant breast cancer treatment as a sensitive setting for trastuzumab biosimilar development and extrapolation," Future Oncol. **11**(1), 61–71 (2015).
5. C. Rousseau, A. Devillers, C. Sagan, L. Ferrer, B. Bridji, L. Campion, M. Ricaud, E. Bourbouloux, I. Doutriaux, M. Clouet, D. Berton-Rigaud, C. Bouriel, V. Delecroix, E. Garin, S. Rouquette, I. Resche, P. Kerbrat, J. F. Chatal, and M. Campone, "Monitoring of early response to neoadjuvant chemotherapy in stage II and III breast cancer by [18F]fluorodeoxyglucose positron emission tomography," J. Clin. Oncol. **24**(34), 5366–5372 (2006).
6. W. F. Symmans, F. Peintinger, C. Hatzis, R. Rajan, H. Kuerer, V. Valero, L. Assad, A. Poniecka, B. Hennessy, M. Green, A. U. Buzdar, S. E. Singletary, G. N. Hortobagyi, and L. Pusztai, "Measurement of residual breast cancer burden to predict survival after neoadjuvant chemotherapy," J. Clin. Oncol. **25**(28), 4414–4422 (2007).

#318127 https://doi.org/10.1364/BOE.9.001375
Journal © 2018 Received 20 Dec 2017; revised 23 Feb 2018; accepted 25 Feb 2018; published 28 Feb 2018

Biomedical Optics EXPRESS

7. S. Aminololama-Shakeri, C. K. Abbey, P. Gazi, N. D. Prionas, A. Nosratieh, C.-S. Li, J. M. Boone, and K. K. Lindfors, "Differentiation of ductal carcinoma in-situ from benign micro-calcifications by dedicated breast computed tomography," Eur. J. Radiol. **85**(1), 297–303 (2016).
8. Y. Zhu, X. Wang, J. Chen, J. Zhang, F. Meng, C. Deng, R. Cheng, J. Feijen, and Z. Zhong, "Bioresponsive and fluorescent hyaluronic acid-iodixanol nanogels for targeted X-ray computed tomography imaging and chemotherapy of breast tumors," J. Control. Release **244**(Pt B), 229–239 (2016).
9. S. Ait-Mohand, V. Dumulon-Perreault, F. Benard, and B. Guerin, "Design optimization of a new 64Cu/NOTA truncated NPY analog with improved stability and Y1 affinity, the first step toward successful breast cancer PET Imaging," J. Nucl. Med. **57**(s2), 1076 (2016).
10. L. L. B. Ponto, Y. Menda, V. A. Magnotta, T. H. Yamada, N. L. Denburg, and S. K. Schultz, "Frontal hypometabolism in elderly breast cancer survivors determined by [(18)F]fluorodeoxyglucose (FDG) positron emission tomography (PET): a pilot study," Int. J. Geriatr. Psychiatry **30**(6), 587–594 (2015).
11. G. J. Wengert, T. H. Helbich, W.-D. Vogl, P. Baltzer, G. Langs, M. Weber, W. Bogner, S. Gruber, S. Trattnig, and K. Pinker, "Introduction of an Automated User-Independent Quantitative Volumetric Magnetic Resonance Imaging Breast Density Measurement System Using the Dixon Sequence: Comparison With Mammographic Breast Density Assessment," Invest. Radiol. **50**(2), 73–80 (2015).
12. S. M. Chung, "Safety issues in magnetic resonance imaging," J. Neuroophthalmol. **22**(1), 35–39 (2002).
13. J. S. Sung and D. D. Dershaw, "Breast magnetic resonance imaging for screening high-risk women," Magn. Reson. Imaging Clin. N. Am. **21**(3), 509–517 (2013).
14. S. A. Boppart, W. Luo, D. L. Marks, and K. W. Singletary, "Optical coherence tomography: feasibility for basic research and image-guided surgery of breast cancer," Breast Cancer Res. Treat. **84**(2), 85–97 (2004).
15. L. Scolaro, R. A. McLaughlin, B. F. Kennedy, C. M. Saunders, and D. D. Sampson, "A review of optical coherence tomography in breast cancer," Photonics Lasers Med. **3**(3), 225–240 (2014).
16. W. M. Allen, L. Chin, P. Wijesinghe, R. W. Kirk, B. Latham, D. D. Sampson, C. M. Saunders, and B. F. Kennedy, "Wide-field optical coherence micro-elastography for intraoperative assessment of human breast cancer margins," Biomed. Opt. Express **7**(10), 4139–4153 (2016).
17. W. Denk, J. H. Strickler, and W. W. Webb, "Two-photon laser scanning fluorescence microscopy," Science **248**(4951), 73–76 (1990).
18. S. W. Perry, R. M. Burke, and E. B. Brown, "Two-photon and second harmonic microscopy in clinical and translational cancer research," Ann. Biomed. Eng. **40**(2), 277–291 (2012).
19. K. Tilbury and P. J. Campagnola, "Applications of second-harmonic generation imaging microscopy in ovarian and breast cancer," Perspect. Medicin. Chem. **7**(1), 21–32 (2015).
20. S. Huang, A. A. Heikal, and W. W. Webb, "Two-photon fluorescence spectroscopy and microscopy of NAD(P)H and flavoprotein," Biophys. J. **82**(5), 2811–2825 (2002).
21. T. M. Cannon, A. T. Shah, and M. C. Skala, "Autofluorescence imaging captures heterogeneous drug response differences between 2D and 3D breast cancer cultures," Biomed. Opt. Express **8**(3), 1911–1925 (2017).
22. A. J. Walsh, R. S. Cook, M. E. Sanders, L. Aurisicchio, G. Ciliberto, C. L. Arteaga, and M. C. Skala, "Quantitative optical imaging of primary tumor organoid metabolism predicts drug response in breast cancer," Cancer Res. **74**(18), 5184–5194 (2014).
23. K. Burke, P. Tang, and E. Brown, "Second harmonic generation reveals matrix alterations during breast tumor progression," J. Biomed. Opt. **18**(3), 031106 (2012).
24. P. P. Provenzano, K. W. Eliceiri, and P. J. Keely, "Multiphoton microscopy and fluorescence lifetime imaging microscopy (FLIM) to monitor metastasis and the tumor microenvironment," Clin. Exp. Metastasis **26**(4), 357–370 (2009).
25. G. Song, D. B. Darr, C. M. Santos, M. Ross, A. Valdivia, J. L. Jordan, B. R. Midkiff, S. Cohen, N. Nikolaishvili-Feinberg, C. R. Miller, T. K. Tarrant, A. B. Rogers, A. C. Dudley, C. M. Perou, and W. C. Zamboni, "Effects of tumor microenvironment heterogeneity on nanoparticle disposition and efficacy in breast cancer tumor models," Clin. Cancer Res. **20**(23), 6083–6095 (2014).
26. C. F. Buchanan, E. E. Voigt, C. S. Szot, J. W. Freeman, P. P. Vlachos, and M. N. Rylander, "Three-dimensional microfluidic collagen hydrogels for investigating flow-mediated tumor-endothelial signaling and vascular organization," Tissue Eng. Part C Methods **20**(1), 64–75 (2014).
27. K. A. Burke, R. P. Dawes, M. K. Cheema, A. Van Hove, D. S. Benoit, S. W. Perry, and E. Brown, "Second-harmonic generation scattering directionality predicts tumor cell motility in collagen gels," J. Biomed. Opt. **20**(5), 051024 (2015).
28. T. Mammoto, A. Jiang, E. Jiang, D. Panigrahy, M. W. Kieran, and A. Mammoto, "Role of collagen matrix in tumor angiogenesis and glioblastoma multiforme progression," Am. J. Pathol. **183**(4), 1293–1305 (2013).
29. S. Wu, H. Li, H. Yang, X. Zhang, Z. Li, and S. Xu, "Quantitative analysis on collagen morphology in aging skin based on multiphoton microscopy," J. Biomed. Opt. **16**(4), 040502 (2011).
30. J. Chen, S. Zhuo, R. Chen, X. Jiang, S. Xie, and Q. Zou, "Depth-resolved spectral imaging of rabbit oesophageal tissue based on two-photon excited fluorescence and second-harmonic generation," New J. Phys. **9**(7), 212 (2007).
31. S. Chakraborty, F.-S. Nian, J.-W. Tsai, A. Karmenyan, and A. Chiou, "Quantification of the metabolic state in cell-model of Parkinson's disease by fluorescence lifetime imaging microscopy," Sci. Rep. **6**(1), 19145 (2016).
32. K. Cai, H. N. Xu, A. Singh, L. Moon, M. Haris, R. Reddy, and L. Z. Li, "Breast cancer redox heterogeneity detectable with chemical exchange saturation transfer (CEST) MRI," Mol. Imaging Biol. **16**(5), 670–679 (2014).

Biomedical Optics EXPRESS

33. B. Chance, B. Schoener, R. Oshino, F. Itshak, and Y. Nakase, "Oxidation-reduction ratio studies of mitochondria in freeze-trapped samples. NADH and flavoprotein fluorescence signals," J. Biol. Chem. **254**(11), 4764–4771 (1979).
34. R. Ambekar, T.-Y. Lau, M. Walsh, R. Bhargava, and K. C. Toussaint, Jr., "Quantifying collagen structure in breast biopsies using second-harmonic generation imaging," Biomed. Opt. Express **3**(9), 2021–2035 (2012).
35. M. J. Koehler, K. König, P. Elsner, R. Bückle, and M. Kaatz, "In vivo assessment of human skin aging by multiphoton laser scanning tomography," Opt. Lett. **31**(19), 2879–2881 (2006).
36. C. W. Huo, G. Chew, P. Hill, D. Huang, W. Ingman, L. Hodson, K. A. Brown, A. Magenau, A. H. Allam, E. McGhee, P. Timpson, M. A. Henderson, E. W. Thompson, and K. Britt, "High mammographic density is associated with an increase in stromal collagen and immune cells within the mammary epithelium," Breast Cancer Res. **17**(1), 79 (2015).
37. J. S. Bredfeldt, Y. Liu, C. A. Pehlke, M. W. Conklin, J. M. Szulczewski, D. R. Inman, P. J. Keely, R. D. Nowak, T. R. Mackie, and K. W. Eliceiri, "Computational segmentation of collagen fibers from second-harmonic generation images of breast cancer," J. Biomed. Opt. **19**(1), 016007 (2014).
38. L. Lam, S.-W. Lee, and C. Y. Suen, "Thinning methodologies-a comprehensive survey," IEEE Trans. Pattern Anal. Mach. Intell. **14**(9), 869–885 (1992).
39. N. Otsu, "Threshold Selection Method from Gray-Level Histograms," IEEE Trans. Syst. Man Cybern. **9**(1), 62–66 (1979).
40. P. P. Provenzano, K. W. Eliceiri, J. M. Campbell, D. R. Inman, J. G. White, and P. J. Keely, "Collagen reorganization at the tumor-stromal interface facilitates local invasion," BMC Med. **4**(1), 38–54 (2006).
41. G. Falzon, S. Pearson, and R. Murison, "Analysis of collagen fibre shape changes in breast cancer," Phys. Med. Biol. **53**(23), 6641–6652 (2008).
42. A. Uppal and P. K. Gupta, "Measurement of NADH concentration in normal and malignant human tissues from breast and oral cavity," Biotechnol. Appl. Biochem. **37**(1), 45–50 (2003).
43. A. J. Walsh, R. S. Cook, H. C. Manning, D. J. Hicks, A. Lafontant, C. L. Arteaga, and M. C. Skala, "Optical metabolic imaging identifies glycolytic levels, subtypes, and early-treatment response in breast cancer," Cancer Res. **73**(20), 6164–6174 (2013).
44. M. W. Conklin, J. C. Eickhoff, K. M. Riching, C. A. Pehlke, K. W. Eliceiri, P. P. Provenzano, A. Friedl, and P. J. Keely, "Aligned collagen is a prognostic signature for survival in human breast carcinoma," Am. J. Pathol. **178**(3), 1221–1232 (2011).
45. J. S. Bredfeldt, Y. Liu, M. W. Conklin, P. J. Keely, T. R. Mackie, and K. W. Eliceiri, "Automated quantification of aligned collagen for human breast carcinoma prognosis," J. Pathol. Inform. **5**(1), 28 (2014).
46. W. Liang, G. Hall, B. Messerschmidt, M.-J. Li, and X. Li, "Nonlinear optical endomicroscopy for label-free functional histology in vivo," Light Sci. Appl. **6**(11), e17082 (2017).

1. Introduction

Breast cancer is the most common form of cancer in women, accounting for about 29% of all new female cancer diagnoses in the United States in 2016 [1]. The diagnosed breast cancer among women is increase of countries worldwide, and with increase per year [2]. It is also the main cause of the cancer-related death in women [2]. Surgical excision of malignant tissue is a central component of traditional breast cancer treatment. Nowadays, neoadjuvant therapy, including chemotherapy and radiotherapy before surgery, is recognized as effective [3, 4]. Researchers have shown that tumor degradation as a result of neoadjuvant therapy can lead to a higher tumor resection success rate, result in reducing the recurrence rate, and improving the survival rate of patients [4–6]. However, with the increasing number of drugs approved to treat cancer, the evaluation of optimal treatment dosage and course for an individual patient is challenging. The potential benefits of the drugs could be outweighed by the side effects in the patient. Therefore, the accurate monitoring of tumor response and the effective evaluation of tumor environment are vital to the individualized treatment of patients. The current gold standard in assessing breast tumor progress and its therapeutic effects is histopathological analysis performed days after surgery, which is invasive and time consuming. Moreover, it is hard to monitor the treatment response in a timely manner after therapy. Hence, there is a critical need for developing new technologies and evaluation methods to predict the efficacy of cancer treatment in individual patients.

Currently, a variety of imaging techniques, such as computed tomography (CT) [7, 8], positron emission tomography (PET) [9, 10], and magnetic resonance imaging (MRI) [11, 12] are used to examine changes in the breast tumors after preoperative chemotherapy, but those examination results are inconsistent with the results of pathological analysis. CT involves a high dose of harmful radiation. PET is widely applied in clinics because of its high sensitivity

Biomedical Optics EXPRESS

and specificity in tissue, but its low spatial resolution and precision limit its ability to reach the subcellular level. PET imaging also requires a contrast agent, which makes it difficult to diagnose many diseases. MRI is widely applied on soft tissue because it does not expose the patient to ionizing radiation and has higher potential for functional imaging than CT or standard radiographs. However, it requires longer scanning time and often results in misdiagnosis as a result of its low spatial resolution. Other limitations to MRI are that it cannot be used on most patients who have implanted medical devices, and some people are allergic to gadolinium contrast [12]. Because of its high false-positive rate, MRI is mainly used as an adjunct to mammography for screening high-risk women with dense breast tissue [13]. Therefore, having a non-invasive, real-time imaging technique that is comparable to pathological analysis is very important for the diagnosis and evaluation of cancers and their therapy. Optical coherence tomography (OCT) and optical coherence elastography (OCE) were applied to study the differences between normal and cancerous breast tissue and have successfully distinguished tumor margins [14–16]. Although OCT has a greater detectable depth, it can only obtain structural information.

Two-photon microscopy (TPM) provides a tool to noninvasively visualize dynamic events and has many advantages, including high resolution, deep penetration depth, and low-level damage to biological tissues [17–19]. There are also many substances in the breast tissue, such as nicotinamide adenine dinucleotide (NADH), flavin adenine dinucleotide (FAD), and elastic fibers that can produce a two-photon excitative fluorescence signal without any external contrast agent [20]. Fluorescence information is useful for characterizing the metabolic properties of normal and abnormal tissues. Cancer metastasis involves complex cell behavior and interactions with the extracellular matrix (ECM) by metabolically active cells. The metabolic rate with autofluorescence (AF) is an important marker for the diagnosis and treatment of breast cancer, and can serve as a general marker of healthy tissue. For example, Skala's group focused on the metabolic changes of cancer drug response [21, 22]. The special noncentral symmetric structure can directly stimulate a second harmonic generation (SHG) signal, such as stromal collagen and tumor-stroma interactions [23]. The tumor microenvironment is composed of ECM proteins, most notably collagen, as well as a wide range of tumor-associated cells [24], including fibroblasts, macrophages, and neutrophils, along with the vasculature. Collagen, which is known to have a significant effect on both mammary morphogenesis and tumor progression, playing an important role in maintaining normal cell behavior due to its control over tumor microenvironment [25–28]. These endogenous signals can be visualized using two-photon imaging to reveal tumor tissue pathological changes, including degradation and stromal fibrosis, which, in turn, could be used to evaluate the effects of treatment after receiving neoadjuvant therapy. This would have a significant effect on tumor prognosis.

In our study, TPM was employed to study normal breast tissue and tumor progression and recession. Study tissue included the normal breast, ductal carcinoma *in situ*, and invasive ductal carcinoma and after neoadjuvant chemotherapy (shortened within text as post-chemotherapy). We analyzed the changes in the tumor microenvironment to reveal the characteristics of the tumor progression and recession. The metabolic activity was obtained from studying NADH intensity, FAD intensity, and optical redox ratio, which are based on endogenous tissue fluorophores that do not require exogenous stains were studied. Then, the collagen content, such as ratio of SHG divided by AF, and collagen density, were calculated to illustrate the tumor progression and recession. Finally, the collagen orientation in different tumors status were extracted to describe collagen distribution.

2. Materials and methods

2.1 Samples

Twenty-three breast tissue samples (seven normal breast samples, six ductal carcinoma *in situ* samples, six invasive ductal carcinoma samples, and four post-chemotherapy samples) were

Biomedical Optics EXPRESS

obtained from 17 patients with ages between 39-to-60 years of age undergoing excision surgery in the Fuzhou First Hospital affiliated to Fujian Medical University. Our protocol was approved by the Institutional Review Board governing clinical investigation of human subjects in biomedical research, and informed consent was obtained from the patients. The neoadjuvant chemotherapy was as follows: docetaxel (75 mg/m^2), doxorubicin (50 mg/m^2), and cyclophosphamide (500 mg/m^2) were combined for intravenous injection. The patients received the drugs on the first day of each of the six 21-day sessions. After chemotherapy, the patients underwent surgery, and the tumor was removed. All the excised tissues taken from each patient was divided into two parts. One part was used for histological diagnoses as the gold standard for reference. The other part was immediately frozen in liquid nitrogen (–196°C) immediately for TPM study. Before the TPM experiment, the samples were cut into 20-μm-thick slices by freezing microtome and then placed on a microscope slide under a cover glass for imaging. To avoid dehydration or shrinkage of samples during the experiment, a few drops of phosphate buffer solution were added before observation.

2.2 TPM system

The experimental system employed in this study has been described previously [29]. The TPM system is a commercial device combined with a Zeiss LSM 510 META laser scanning microscope (Carl Zeiss Microscopy GmbH, Jena, Germany) and a Coherent Mira 900-F mode-locked femtosecond Ti:sapphire laser (Coherent Inc, Santa Clara, CA, USA). Excitation was achieved using a tunable Ti:sapphire laser emitting 110 fs pulses at 76 MHz. The excitation wavelengths at 810 nm, 830 nm, and 850 nm were all good to obtain collagen images in our experiments. It was verified that the 810 nm excitation wavelength was the optimal excitation wavelength for producing a mitochondrial signal of NADH and FAD [30]. So, the excitation wavelength was set at 810 nm with an average power ~10 mW. To eliminate the influence of experimental conditions, all the experiment settings were consistent for each sample. An oil immersion objective (Plan-Apochromat 63 NA 1.4, Zeiss; Carl Zeiss Microscopy GmbH) was used. The SHG signal was detected at 404 nm with a bandwidth of 20 nm, while the AF signal was detected from 430 nm to 714 nm.

2.3 Data analysis

2.3.1 Spectrum and oxidation-reduction (redox) ratio

The AF spectrum provides powerful information that contains various endogenous fluorophores, such as NADH, NADPH, elastin, flavins, and others. The endogenous fluorophores NADH and FAD are two AF cofactors that act as electron donors and acceptors in cellular metabolism [31, 32]. Their concentrations can be detected using TPM. The 32 META channels detector recorded some peaks in the spectrum with 405 nm, 475 nm, 511 nm, and 540 nm, which indicated collagen, NADH (NADPH), elastin, and FAD, respectively [30]. As first reported by Chance, the mitochondrial redox state can be obtained by measuring the NADH and FAD [33]. The optical redox ratio is defined as the intensity of NADH divided by the intensity of FAD, and represents cellular metabolism [22]. The NADH and FAD redox index reflects the activity of the mitochondrial electron transport chain, as well as tissue metabolism [31]. In our study, we focused on optical redox in the ductal tissues, including normal ductal tissue, ductal carcinoma *in situ,* and ductal carcinoma *in situ* post-chemotherapy (the samples included in the invasive ductal carcinoma samples).

2.3.2 Collagen content with SHG/AF and collagen density

Collagen is an important and abundant ECM component that can generate intrinsic contrast via SHG, which has been used to visualize collagen structures in many disease states [34]. Collagen content can be used to identify the degree of tissue abnormality. In our study, the intensity of SHG divided by the intensity of AF was obtained [35]. This value shows the

Biomedical Optics EXPRESS

content of SHG and AF, and can reflect changes in the microenvironment. Collagen density is another parameter for testing collagen content, which is similar to mammary gland density because collagen is an important component of normal breast tissue [36]. The collagen density reflects the changes in collagen in different tissues. The collagen density value was obtained by calculating the ratio of the number of pixels containing collagen divided by the number of pixels in the whole image in the extent scale image obtained from TPM in the SHG channel. The SHG images only contain only SHG information, while the AF information, including about the other endogenous fluorophores, was displayed in black in the SHG images.

2.3.3 Collagen orientation based on a center line

Quantitative analysis of collagen fiber shape orientation is key to characterizing abnormal tissue [37]. There are some methods available for obtaining the collagen shape or alignment [37]. In this paper, the fiber orientation is derived from a center line-based algorithm [38]. This algorithm first skeletonizes a binary image of the fibers. Orientation was then estimated using the tangent line of each pixel along the skeleton (center line). The orientation of the tangent line was estimated using the positions of the start and end points of the center line intersecting the window boundaries. Compared with other methods, such as Fast Fourier Transform, the center line method is better at ignoring the crudeness or fineness of the collagen fiber. The results ignore the collagen dimension and can be automatically computed.

Otsu's threshold is an unbiased threshold that optimizes the ratio of between-group to within-group variance, and it was employed to generate the binary image and segment the fiber bundles [39]. The binary image of fiber bundles was then shrunk to a center line based on the thinning algorithm and became a skeletonized image [38]. After that, a small square window of size $(2N + 1) \times (2N + 1)$ was created to evaluate the tangent orientation at each pixel in the skeleton, where 2N is the number of directions around the center. The line passing through the start and end points of the center line on the window edge can be treated as the tangent line when the window center is $(N + 1, N + 1)$ because of the small window size. Then, a start point (x_1, y_1) and an end point (x_2, y_2) were applied for extracting the slope k of the tangent line, which can be expressed as:

$$k(i,j) = (y_2 - y_1)/(x_2 - x_1), if\ x_2 - x_1 \neq 0 \tag{1}$$

The corresponding orientation θ was given by:

$$\theta(i,j) = \begin{cases} arc\tan k(i,j), if\ k \geq 0 \\ \pi + arc\tan k(i,j), if\ k < 0 \\ \pi/2, \qquad if x_2 - x_1 = 0 \end{cases} \tag{2}$$

All orientation values are within the range of (0, 180] deg.

The size of the fiber could be quantified using the radius, where the local radius for every pixel (s) on the skeleton was defined to be the minimal distance between the skeleton and pixel b on the boundary set (B) in the binary image,

$$R(b) = \min\left[\underset{\forall b \in B}{dist}(s,b)\right] \tag{3}$$

For pixels located between the boundary and the skeleton, the orientations were approximated as the corresponding orientation at the point S extracted in the skeletonized image. Thus, the orientations between the boundary and skeleton were equal and the number of orientations could be calculated using the areas between the boundary and skeleton, which was $R \times L$, where L is pixel size. When the skeleton set S fell at the ends of the skeleton, the number of orientations (No) was approximated as

Biomedical Optics EXPRESS

$$N_o = \pi R_a^2 / 2 \quad (4)$$

Where R_a is the radius at the ends of the skeleton. Thus, the orientation was merged with the skeletonized image by combining it with the number of corresponding orientations for quantifying the orientation distribution in the whole image. The probability density function was estimated from a histogram of spatially resolved orientations ranging from 0 deg to 180 deg, and statistical parameters including the mean and the standard deviation of orientation were also calculated.

2.3.4 Statistical analysis

Five images from regions of interest (ROI) in different positions of each sample were obtained for quantitative analysis. A two-sample t-test with unequal means was completed to determine whether the difference was significant in the statistical parameters between any two sample groups. Differences were regarded as statistically significant when $p<0.05$.

3. Results and discussions

3.1 Breast cancer structure

Representative images of normal breast tissue, ductal carcinoma *in situ*, invasive ductal carcinoma, and invasive ductal carcinoma post-chemotherapy obtained from TPM are displayed in Fig. 1.

The images in the first column (A1, B1, C1, and D1) were obtained from the intrinsic fluorescence resulting mainly from fluorophores such as NADH, elastin, or FAD in the above four types of tissues, respectively. In Fig. 1(A1), the high intensity region (red) is the mammary gland lobule, which has strong AF signals. In the extraductal stroma, there is very little AF signal. From Fig. 1, it is obvious that the intensity of AF in the stromal region increases with tumor progression (e.g. ductal carcinoma *in situ* [B1] and invasive ductal carcinoma [C1]), and decreases slightly post-chemotherapy (D1). These changes indicate that cancer progression causes more AF signals. Because the nuclei are largely devoid of any AF, they appear as empty within the cell. Thus, information about cell nucleus cannot be obtained from TPM imaging, as the nuclei appeared black in images.

The collagen obtained from SHG microscopy of the four different samples status is displayed in the second column (A2, B2, C2, and D2). The morphology of collagen differs in each of the sample status, especially in intensity and fiber shape. Collagen is an indicator of tissue lesion, and collagen structure/character play an important role in maintaining normal tissue function [40]. Thus, SHG has been used to visualize collagen structures in many disease states. Collagen is generally rod-like, and the differences in shape among the four tissues types (normal breast, ductal carcinoma *in situ*, the invasive ductal carcinoma, and post-chemotherapy) are easy to distinguish [37, 41]. It is evident that the collagen fiber is bundled and has a large degree of curvature in the normal extraductal breast tissue. The mammary gland lobule is surrounded by collagen, as shown in Fig. 1(A2), and the intensity of SHG is very strong where the AF signal intensity is low. However, in the ductal carcinoma *in situ* sample, the collagen fiber shape became thinner, longer, and less curvature (Fig. 1(B2). The collagen near the duct is fractured in some regions, most likely because of the destruction and loss of collagen during tumor progression. This phenomenon is more evident in invasive ductal carcinoma, as the carcinoma cells can break through the duct to invade the stromal matrix, as shown in Fig. 1(C2). The collagen here is thin, long, and straight. The strong collagen signal intensity decreases sharply, while the AF signal increases in the extraductal stromal region in this tissue status. Collagen structure in invasive ductal carcinoma post-chemotherapy is seen in Fig. 1(D2). The collagen is more bundled than in invasive ductal carcinoma. The intensity and quantity of collagen in invasive ductal carcinoma and post-chemotherapy are greatly changed, although the tumor structure characteristic is still

Biomedical Optics EXPRESS

preserved in the tissue. The phenomena could be explained by the destruction of collagen by carcinoma cells and its collagen regeneration due to chemical drug therapy.

The combination of AF and SHG is displayed in the third column of the Fig. 1(A3, B3, C3, and D3). It provides a more comprehensive view of the changes in SHG and AF images during breast cancer progression and chemotherapy.

The fourth column in the Fig. 1(A4, B4, C4, and D4) are the corresponding hematoxylin and eosin (H&E) stained histological images of the four samples status. The pink areas are collagen. The structures from TPM match well with the histopathological images.

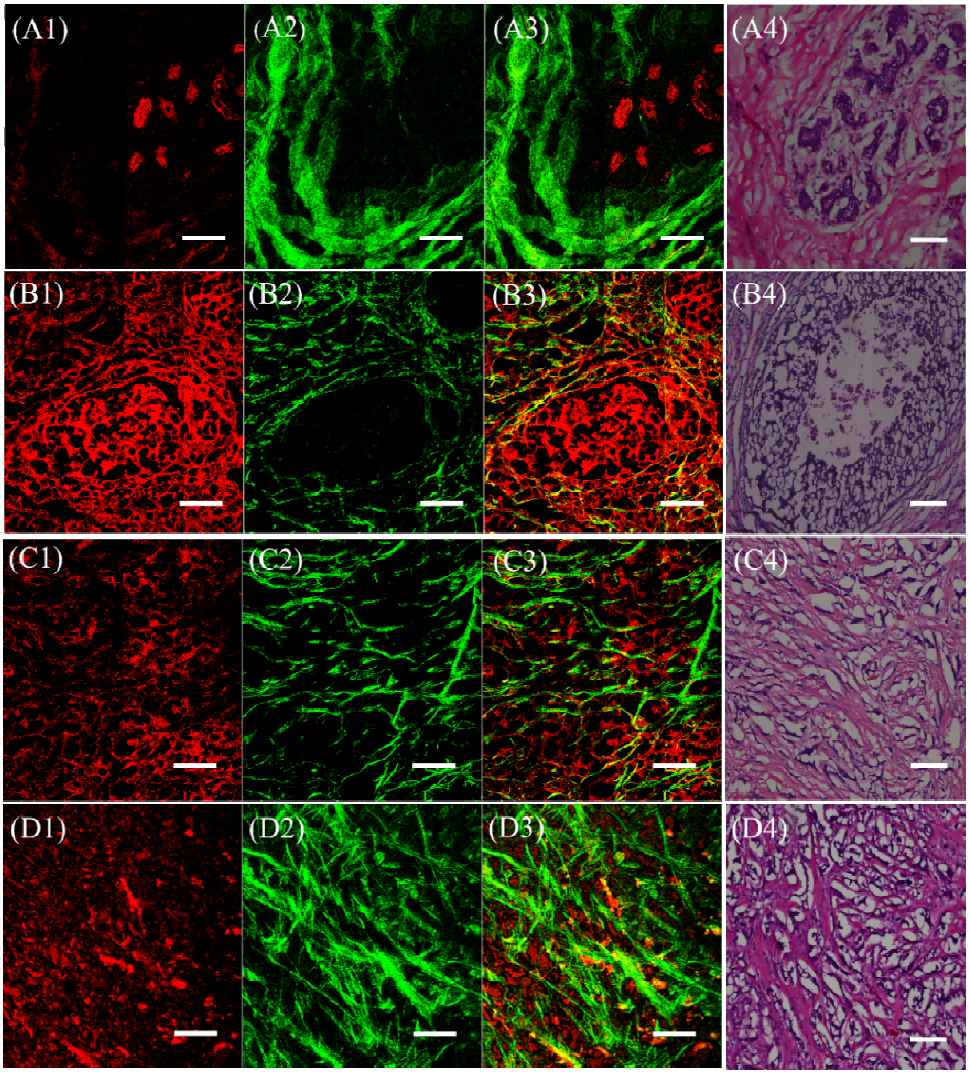

Fig. 1. TPM images and histological images of the structures of breast tissues in four samples status. The first column (A1, B1, C1, and D1) was obtained by AF, which reflects endogenous fluorophore. The second column (A2, B2, C2, and D2) was obtained by the second harmonic generated, which reflects the collagen. The third column (A3, B3, C3, and D3) combines AF and SHG. The fourth column (A4, B4, C4, and D4) is the corresponding H&E stained images. (A1) -(A4) Normal breast, (B1) -(B4) Ductal carcinoma *in situ*, (C1) -(C4) Invasive ductal carcinoma, and (D1) -(D4) Invasive ductal carcinoma post-chemotherapy. The scale bar is 100 μm.

Biomedical Optics EXPRESS

3.2 Breast cancer redox ratio

In this study, spectral images were obtained from 382 nm to 714 nm with 32 channels and an 11-nm interval using the lambda mode of the TPM, as shown in Fig. 2(A). The combined image of 32 channels is shown in Fig. 2(B). The spectrum data with 32 channels was obtained by further analyzing the mean value of the ROI. The normalized spectrum distribution in intraductal regions of different samples status is displayed in Fig. 2(C). The 404-nm channel shows the collagen, the 479-nm channel shows the NADH, and the 543-nm channel shows the FAD from the ROI. The spectrum distribution changed greatly in different samples status. The normal breast data was obtained from the intraductal region with many breast cells, which are surrounded by collagen. The SHG spectrum intensity, however, is very weak, while the AF is strong in this region. This is mainly caused by the dense breast cell distribution in the ductal region. In ductal carcinoma *in situ*, the SHG intensity is very weak, but AF is greater than normal because of the abundant endogenous fluorophores. The cancer cells were destroyed and the AF intensity is reduced post-chemotherapy. This most likely was caused by the response to chemotherapeutic drugs.

It has been reported that the metabolic redox rate changes in breast cancer tissues [22]. Monitoring the metabolic changes at cellular level is important for understanding the disease processes, and the effect of therapies. NADH intensity, FAD intensity, and optical redox were calculated as quantitative parameters to characterize the breast cancer's metabolism and the effects of chemotherapy. The results are displayed in Fig. 2(D) and (E).

From Fig. 2(D) illustrates that as cancer progressed, NADH and FAD intensities increased sharply in ductal carcinoma *in situ*, and were reduced post-chemotherapy. We observed that NADH intensity is about 1.6 times higher in ductal carcinoma *in situ* than that in normal tissue. The results are consistent with findings from other researchers [42]. Post-chemotherapy, NADH intensity decreases, but the value is still higher than that in normal tissue. The tendency for variation in FAD intensity is similar, but the amplitude of it is smaller than for NADH. FAD intensity is about 1.4 times higher in ductal carcinoma *in situ* than that in normal breast tissue, and it decreases post-chemotherapy. The decrease in NADH and FAD intensity may also be caused by the drug's response.

The optical redox ratio (NADH /FAD), is displayed in Fig. 2(E). In our study, the optical redox ratio increases in tumor status. The result is consistent with the literature [33]. Post-chemotherapy, the optical redox ratio decreases, but the values are still higher than the normal levels. It shows the response of drug on cancer. The greater the reduction of optical redox, the more effective the neoadjuvant treatment. The result is consistent with another reported study [43]. The data shows that there is a significant difference in optical redox ratio between normal, ductal carcinoma *in situ*, and post-chemotherapy of ductal carcinoma *in situ*.

Breast tumor tissue has a higher cell density than normal breast tissue. The cell density is reduced post-chemotherapy. This reduction is caused by the drug(s). This might provide some clues for the genesis of higher FAD and NADH concentrations in cancerous tissues and the decreasing trend post-chemotherapy. The increase in the optical redox ratio indicates increased cellular metabolic activity during cancer progression, while the decrease in optical redox ratio implies decreased cellular metabolic activity going along with the drug response. The results indicate that the optical redox value is sensitive to cancer progression and treatment.

Biomedical Optics EXPRESS

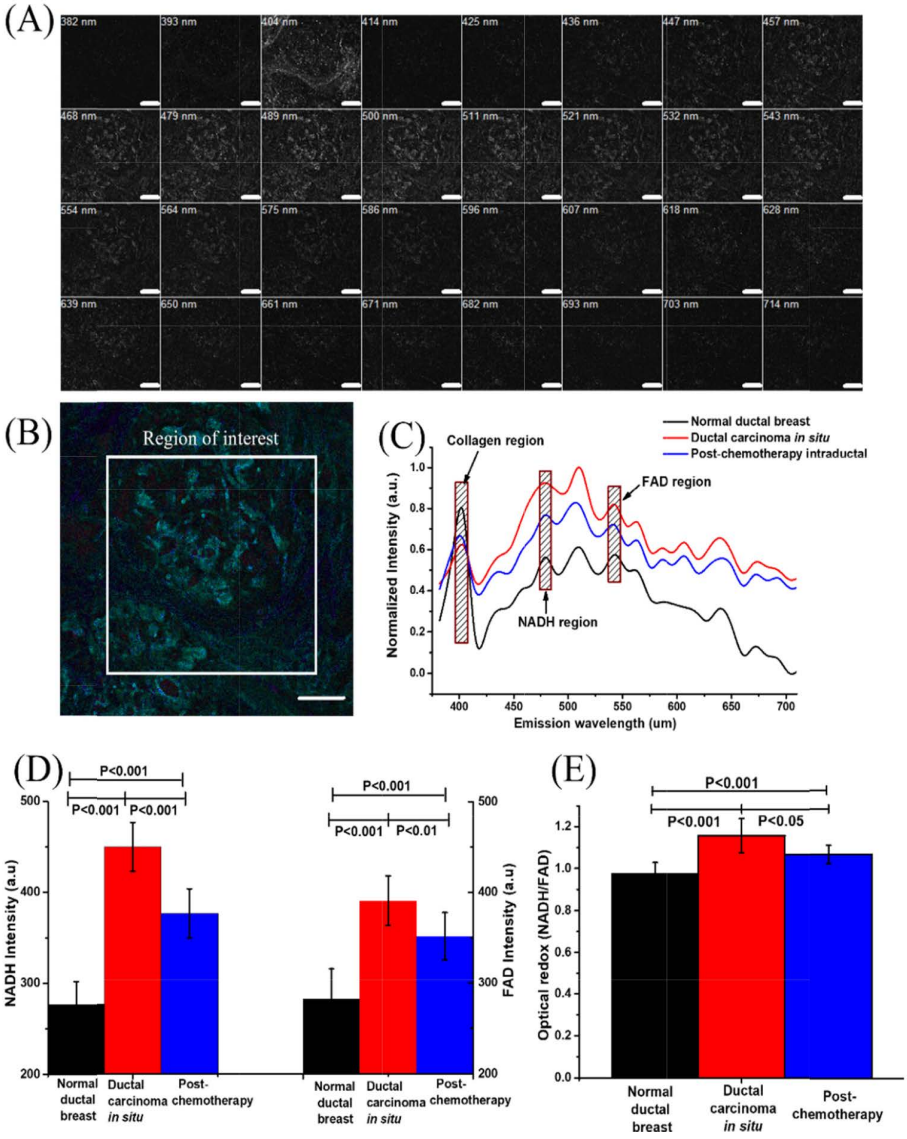

Fig. 2. Spectral information and the redox ratio in the breast tissues. (A) Lambda mode imaging of a breast tissue with 32 channels. The SHG channel is at 404 nm; the NADH channel is at 479 nm; the FAD channel is in the 543-nm channel. (B) The combined imaging of lambda mode. (C) The normalized intensity vs. the emission wavelength with collagen, NADH, and FAD highlighted respectively. (D) NADH and FAD intensities, as well as (E) the optical redox in three breast tissues status. The samples for statistics include seven normal intraductal breast, six ductal carcinoma *in situ* and four ductal carcinoma post-chemotherapy. The scale bar is 100 μm.

3.3 Breast cancer collagen content

Collagen is an important and abundant ECM component that can generate intrinsic contrast via SHG, which denotes the different structures in many disease states. Microenvironmental changes in the tumor are primarily connected with the changes in collagen within the tissue stroma. From the images and the intensities analyzed above, we notice that there is little collagen in the breast ducts. Herein, seven extraductal regions from normal breast tissue samples, six invasive ductal carcinoma samples, and four invasive ductal carcinoma post-

Biomedical Optics EXPRESS

chemotherapy were taken for study. The SHG images are shown in Fig. 3(A), (B), and (C), respectively. The corresponding AF images are shown in Fig. 3(D), (E), and (F).

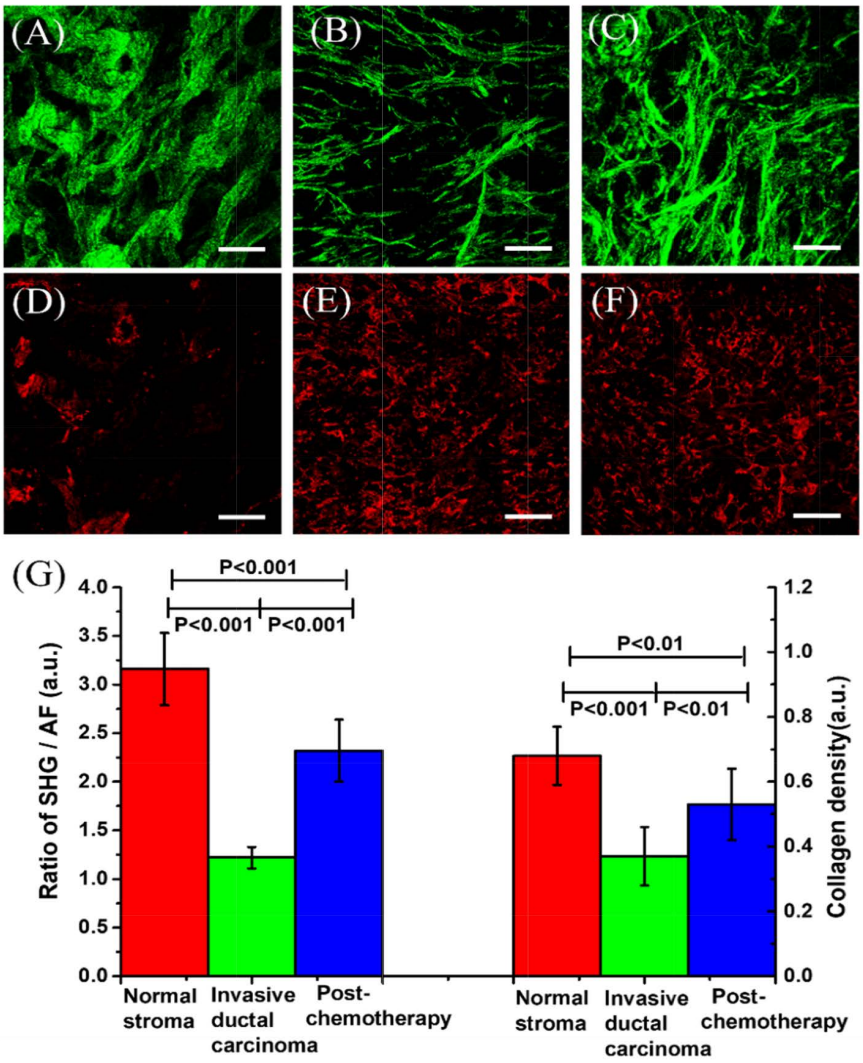

Fig. 3. The collagen intensity in different tissues status. (A)–(C) Images of collagen: (A) Normal stroma, (B) Invasive ductal carcinoma, (C) Post-chemotherapy. (D)-(F) AF images: (D) Normal stroma, (E) Invasive ductal carcinoma, (F) Post- chemotherapy. (G) The ratio of SHG/AF and the collagen density of the three status of breast tissues. The samples include seven normal stroma breast, six invasive ductal carcinoma and four post-chemotherapy. The scale bar is 100 μm.

To quantitatively analyze the collagen content, the SHG/AF ratio and collagen density were considered as biomarkers to reflect the process of tumor progression and recession post-chemotherapy. The SHG/AF and the collagen density were obtained using the method described in methods. The results for SHG/AF and collagen density from the three breast tissues status are shown in Fig. 3(G). The value of SHG/AF is about 3.26 ± 0.37 in normal

Biomedical Optics EXPRESS

breast stroma, and the value decreases to about 1.22 ± 0.11 in invasive ductal carcinoma, and then increases to about 2.37 ± 0.32 post-chemotherapy. The collagen density value is about 0.68 ± 0.09 in normal breast tissues, decreases to 0.37 ± 0.06 in invasive ductal carcinoma, and increases to 0.53 ± 0.08 post-chemotherapy. All these values have a statistically significant difference. The results indicate that the collagen content is high in normal breast, and decreases sharply in invasive ductal carcinoma, and then increases post-chemotherapy. These results indicate that the collagen was destroyed after carcinoma cell invasion and regenerated after chemotherapy. Hence, the collagen regeneration can be considered to be an indicator of cancer recession. These parameters can be used to monitor and assess the effects of chemotherapy. In our study, the significant differences between the values for normal stroma and post-chemotherapy imply that the therapy had some effects but the tissues have not yet recovered to the normal.

3.4 Breast cancer collagen orientation

Recent studies have shown that collagen fiber alignment plays an important role in breast cancer progression [44, 45], and potentially can be used to predict therapy outcome. The autocalculated fiber orientation method was described in "Methods". The merit of this method is that the results are not associated with the collagen's dimensions in different tissues status. The process of extracting the value of orientation is displayed in Fig. 4.

Figure 4(A) is the gray-scale image of normal breast. Figure 4(B) is the binary image of Fig. 4(A). Figure 4(C) is the image after filtering. Figure 4(D) is the center line image obtained based on the thinning algorithm. The fiber orientation value was then obtained through the method described previously. Figure 4(E), (F), (G), and (H) are the center line images of normal breast, ductal carcinoma *in situ*, invasive ductal carcinoma, and post-chemotherapy, respectively. We analyzed the distribution of the mean values of fiber orientation with images rotated from 0 to 180 degrees as shown in Fig. 4(I). The mean value of the fiber orientations changes greatly with the image rotation, while the standard deviation (SD) remains stable with different rotation angles. The mean value of the fiber orientations is related to the direction of sample placement. SD denotes the magnitude of deviation from the mean. A high SD value indicates large fluctuations in orientation, while a low SD value denotes small fluctuations in the angle, which suggests a more consistent orientation. The SD value was taken as a parameter for evaluation of the orientation in the four status of breast tissues, as shown in Fig. 4(J). The SD value of fiber orientation in normal breast tissue is about 53.2 ± 3.2 degrees. The value decreases to about 37.7 ± 2.3 degrees in ductal carcinoma *in situ*, and increases to about 38.2 ± 1.7 degrees in invasive ductal carcinoma. Post-chemotherapy, the value increases to about 42.1 ± 2.8 degrees. The results indicate that in normal breast tissue, the collagen orientation varies more, suggesting a curved collagen fiber shape. In carcinoma tissue, the collagen orientation varies less, suggesting a much straighter collagen fiber shape. These results are consistent with Falzon et al.'s research regarding the shape of collagen in breast cancer progression [41]. Post-chemotherapy, the increased SD value of collagen orientation implies that the collagen fibers become more curved.

Our method is automated for evaluating the orientation of collagen. Moreover, the center lines used to identify the collagen fiber orientation are independent from the dimension of the collagen. This is helpful, as the fiber thickness in normal and abnormal tissue may vary. The results may be used to develop an emerging method of collagen orientation-related tumor biomarkers. These biomarkers have the potential to aid in rapid and precise evaluation of cancer therapy. They may also aid physicians in formulating effective therapeutic plans to improve patient clinical outcomes.

Biomedical Optics EXPRESS

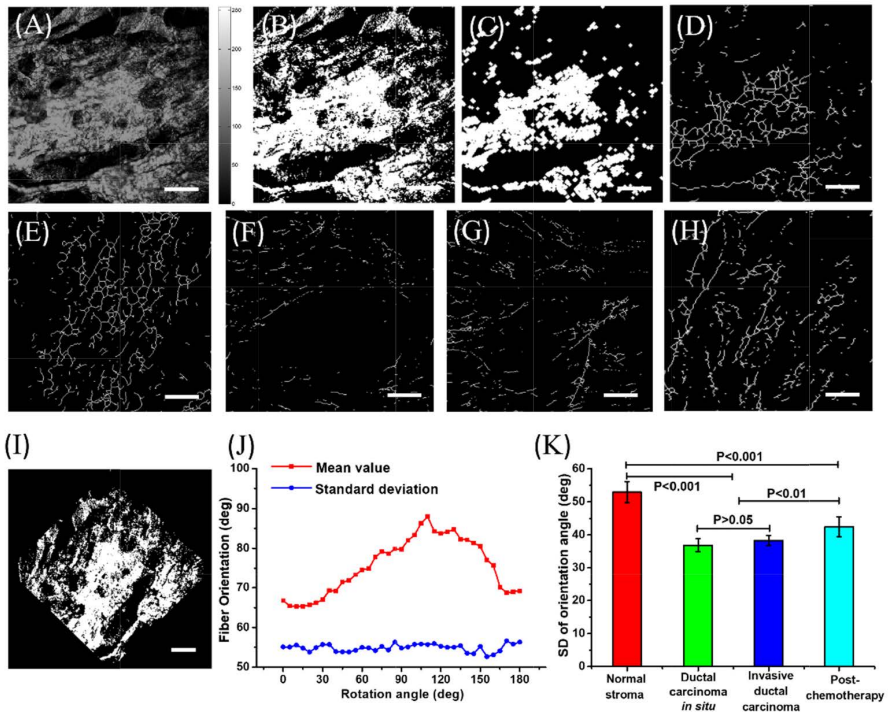

Fig. 4. Collagen orientation information for the four breast tissues status extracted from the collagen center line. (A) A breast tissue SHG image. (B) The binary image of (A). (C) The filtered image. (D) The center line image. (E) The center line image of normal breast tissue. (F) The center line image of ductal carcinoma *in situ*. (G) The center line image of invasive ductal carcinoma. (H) The center line image of invasive ductal carcinoma post-chemotherapy. (I) The normal breast image rotated by 45 degrees. (J) The mean and SD values of fiber orientation with different rotation angles. (K) The standard deviation of fiber orientation in breast tissues with different status. The statistical samples include seven normal stroma breast tissues, six ductal carcinoma *in situ* samples, six invasive ductal carcinoma samples and four post-chemotherapy samples. The scale bar is 100 μm.

4. Conclusions

In this study, we investigated the changes in tissue ultrastructure and tumor microenvironment during breast tumor progression and its recession through TPM. In invasive ductal carcinoma, the collagen content is reduced and its shape morphs into a thin line. Using SHG signal, we observed some fragments of collagen. Post-chemotherapy, the tumor underwent a fibrosis reaction, in which the tumor tissues were replaced by a small amount of collagen fibers.

A series of parameters, including NADH intensity, FAD intensity, and optical redox for analyzing the redox of tissue, and ratio of SHG / AF, collagen density for analyzing the collagen content, and collagen fiber orientation for analyzing the shape of collagen, were extracted for evaluating normal breast tissues, breast cancer tissues (ductal carcinoma *in situ* and invasive ductal carcinoma), and the breast cancer tissues post-chemotherapy. The results showed that tissue with carcinoma exhibits a high metabolic rate. Collagen content changes also play an important role in the process of tumor progression and recession. The ratio of SHG/AF and collagen density showed that the collagen degenerates with the tumor progression, while post-chemotherapy, the collagen regenerates. The orientation of collagen,

Biomedical Optics EXPRESS

extracted from the center line, can be used to reflect the changes in the shape of collagen in breast tissues with different samples status.

Although the study was on a small number of samples, these results indicate that the parameters observed may have great potential for monitoring breast tumor progression and response to chemotherapy through TPM. We believe that by bringing a recently developed two-photon endoscopic technology [46] into a clinical setting, the parameters that can be monitored will aid clinicians in deciding course of therapy, determining the need for surgical intervention, and identifying the pathological reaction while avoiding inappropriate or excessive treatments. This could truly personalize breast cancer treatment monitoring and evaluation.

Funding

National Natural Science Foundation of China (NSFC) (61675043/81571726); Changjiang Scholars and Innovative Research Team (IRT_15R10).

Acknowledgments

Authors acknowledged Prof. Jianxin Chen, from Fujian Normal University, for experimental setup support.

Disclosures

The authors declare that there are no conflicts of interest related to this article.